FEATURE ARTICLE

Harnessing Surface Wrinkle Patterns in Soft Matter

By *Shu Yang,* Krishnacharya Khare,* and *Pei-Chun Lin*

Mechanical instabilities in soft materials, specifically wrinkling, have led to the formation of unique surface patterns for a wide range of applications that are related to surface topography and its dynamic tuning. In this progress report, two distinct approaches for wrinkle formation, including mechanical stretching/releasing of oxide/PDMS bilayers and swelling of hydrogel films confined on a rigid substrate with a depth-wise modulus gradient, are discussed. The wrinkling mechanisms and transitions between different wrinkle patterns are studied. Strategies to control the wrinkle pattern order and characteristic wavelength are suggested, and some efforts in harnessing topographic tunability in elastomeric PDMS bilayer wrinkled films for various applications, including tunable adhesion, wetting, microfluidics, and microlens arrays, are highlighted. The report concludes with perspectives on the future directions in manipulation of pattern formation for complex structures, and potential new technological applications.

1. Introduction

Instabilities are commonly manifested in our daily lives, such as in water jets breaking into isolated drops, wave patterns at the sea surface, sand dunes, cloud waves, ruptures of paint from a wall, and wrinkles on human skin. These occur when the materials system is under both equilibrium and non-equilibrium states. Some of the instabilities are elastic in nature such that they can disappear/reappear by the application of an external force. Previously, such elastic instabilities in soft materials, including liquids, elastomers, elastoplastic polymers, and hydrogels, had often perceived as failure mechanisms. Recently these instabilities have been exploited to assemble complex patterns,[1–6] to fabricate novel electronic devices,[7,8] diffraction gratings,[9] and microlens arrays,[10,11] to tune surface wetting[12–14] and adhesion,[15,16] and to switch photonic[17] and phononic properties,[18] as well as to provide a metrology for measuring mechanical properties of ultrathin films.[19–21]

[*] Prof. S. Yang, Dr. K. Khare[+]
Department of Materials Science and Engineering
University of Pennsylvania
3231 Walnut Street, Philadelphia, PA 19104 (USA)
E-mail: shuyang@seas.upenn.edu
Dr. P.-C. Lin
Department of Mechanical Engineering
National Taiwan University
No. 1, Sec. 4, Roosevelt Road, Taipei, 10617 (Taiwan)
[+] Current address: Department of Physics, Indian Institute of Technology Kanpur, Kanpur – 208016 (India)

DOI: 10.1002/adfm.201000034

In these applications soft materials are often in the form of thin films, whose physical properties can deviate substantially from their bulk counterparts. Here, mechanical properties of thin polymer films play a key role in generating instabilities in the films, thus controlling surface pattern formation and evolution. Over the last several decades numerous theoretical and experimental studies have been performed to understand and manipulate various elastic instabilities, including wrinkling,[2,22] creasing,[1,23–25] and crumpling.[26] In general, confinement of a soft liquid[27,28] or a soft solid[29,30] surface under an external field or residual stress[31,32] engenders the surface instability, leading to self-organized patterning of the film surface. For example, when the surface of a soft elastomeric film, such as poly(dimethylsiloxane) (PDMS), is brought in contact with a flat rigid surface, an instability occurs leading to surface corrugation with a characteristic wavelength of the pattern that is nearly independent of the external force, but varies linearly with the film thickness.[30,33] In contrast to elastic instability, where the material system shifts between different "stable" equilibrium states, kinetic instability is a dynamic process, which depends on the viscoelasticity of the materials, solvent diffusion rate, the pressure, and the rate of force applied to the film. For example, hydrodynamic-force-driven non-equilibrium systems give rise to many different instability patterns, ranging from simple finger-like[28,34] to Marangoni patterns,[35,36] to highly exotic dendritic fractals.[37,38] Among them, the simplest system is Saffman-Taylor instability,[39] an analog of the Rayleigh-Taylor instability. When a low-viscosity fluid displaces a high viscosity fluid between two parallel plates, the interface becomes unstable due to surface tension induced pressure difference at the interface. To stabilize the perturbations, fingering in the moving interface is developed. For many technological applications, it will be important to control the instabilities and guide the pattern formation. Electrostatic forces have been used to induce formation of ordered lateral structures, as well as hierarchical patterns on the surface of polymer thin films, depending on the surface topography of the electrodes.[40,41]

When a thin film confined on a rigid flat substrate is exposed to a solvent, residual stress in the thin film will build up due to anisotropic swelling within the film. Although the film is initially isotropic, because it is fixed on a rigid flat substrate, only the top layer is free to expand, thus generating an anisotropic osmotic pressure along the film thickness. When the stress exceeds a critical value, the outer surface is forced to buckle into distinct surface patterns, where the equilibrium morphology

is determined by the mechanical properties of the film (e.g., crosslinking density or modulus and initial film thickness), whereas the characteristic wavelength of the pattern is controlled by the initial film thickness.[1,24,42] Southern and Thomas reported the formation of surface wrinkles (actually creases) when a rubber film bonded on a steel plate was swollen in various organic solvents.[43] Later, Tanaka et al.[1] observed kinetic evolution of swelling-induced surface patterns, i.e., creasing instability, in ionized poly(acrylamide) ionic hydrogels cast in a petri dish. The osmotic pressure was found to increase with time as the gel swells and the pattern formation was transient in nature depending on the osmotic pressure. Since the landmark work by Tanaka et al. many have attempted to manipulate the surface pattern formation in various hydrogels both experimentally[24,42,44–46] and theoretically.[47–53] Nevertheless, control of the long-range order and morphology of the final wrinkling patterns remain elusive due to the nonlinear nature of the gel swelling. Recently a few groups have explored the diffusion-controlled swelling-induced instability in different polymer films coated with a hard thin layer to create a variety of complex patterns[54,55] and by introduction of a depth-wise crosslinking gradient in the hydrogel film.[42,56]

Alternatively, one can generate wrinkling instability by buckling a bilayer system, where a thin hard film coated on top of an expanded soft substrate (e.g., PDMS) undergoes a compressive force. The compressive strain in the top layer can be provided either by applying a mechanical strain[19,20,57–59] or by shrinking (expanding) its present state than its equilibrium stress-free state by lowering (raising) the temperature or application of a solvent.[2,10,21,42,54]

Here, we overview the recent advances in fabrication of various surface wrinkling patterns and the manipulation of pattern transition and evolution. We then highlight some of our efforts in harnessing wrinkle patterns for various applications, including tunable adhesion, wetting, open-channel microfluidics, and responsive microlens arrays.

2. Wrinkling Instability in a PDMS Bilayer System

2.1. Mechanism of Surface Wrinkling

When a thin elastic film is coated on top of a pre-strained soft substrate (e.g., PDMS), followed by release of the pre-strain, the bilayer system can undergo a buckling instability due to mismatch in the equilibrium states of both layers (**Figure 1**), leading to the formation of various wrinkling patterns on different length scales, where the system arrives in a new equilibrium state. This can be explained by considering the soft substrate as a large spring, where the rest length indicates equilibrium state with minimum energy. When expanded, for example, by heat or mechanical stretching, external energy input is partially transformed into potential spring energy within substrate. After coating a thin hard layer on the soft substrate, followed by application of a compressive force (e.g., cooling the sample down or by release of the mechanical stretch), a new equilibrium state must be relocated due to mismatch of two equilibrium states between the soft elastomeric substrate and the hard elastic

Shu Yang is an Associate Professor in the Department of Materials Science and Engineering at University of Pennsylvania. She received her B. S. degree in Materials Chemistry from Fudan University, China in 1992, and Ph. D. degree from Chemistry and Chemical Biology with Professor Christopher K. Ober at Cornell University in 1999. She then joined Bell Laboratories, Lucent Technologies as a Member of Technical Staff before moving to Penn in 2004. Her research interests include synthesis and engineering of well-defined polymers and inorganic materials with controlled size, shape, and morphology over multiple length scales, study of their directed assembly and unique surface, optical, and mechanical properties, as well as dynamic tuning.

Krishnacharya Khare obtained a MS degree in Physics from the Indian Institute of Technology Delhi, India in 2003. After receiving his PhD in Physics in 2007 with Professor Stephan Herminghaus from Max-Planck Institute, Göttingen, Germany, he joined the Materials Science and Engineering Department of the University of Pennsylvania, USA, as a postdoctoral fellow with Professor Shu Yang. Since returning to India in 2009, he has been working as an Assistant Professor in the Physics Department at the Indian Institute of Technology Kanpur. His research interest involves smart responsive surfaces, tunable wettability and superhydrophobicity, and mechanical properties of soft materials.

Pei-Chun Lin is an Assistant Professor in the Department of Mechanical Engineering at National Taiwan University (NTU), Taipei, Taiwan. He received his B.S. and M.S. degrees in Mechanical Engineering from NTU in 1996 and 1998, respectively, and Ph.D. degree in Mechanical Engineering from The University of Michigan, Ann Arbor, USA in 2005. He then worked with Professor Yang as a postdoctoral research fellow before moving to NTU in 2007. His research interests include bio-inspired robotics, mechanical design, sensor design/fusion, control, locomotion, and tunable polymers.

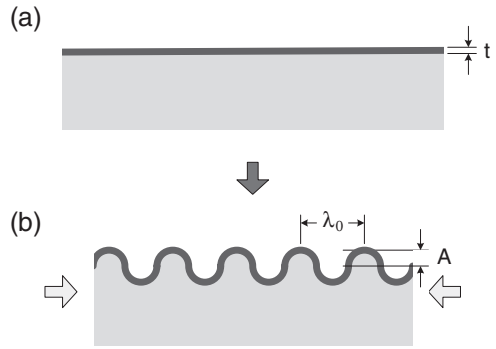

Figure 1. Schematics of wrinkle formation through buckling instability in a bilayer system.

surface layer when the substrate spring force exceeds the critical threshold for buckling the surface thin layer. The wrinkle wavelength and amplitude is the result of minimization of the total elastic energy in the thin layer and the soft substrate.[51] Wrinkling relaxes the compressive strain in the thin hard layer, thus reducing the energy. At the same time, it bends the thin layer, which increases the elastic strain energy.

The wavelength λ_0 of the wrinkling pattern depends on the thickness of the thin hard film t and the mechanical properties of the thin film and the substrate[19,57,60–63] as predicted by linear bulking theory,

$$\lambda_0 = 2\pi t \left(\frac{\overline{E}_f}{3\overline{E}_s} \right)^{1/3} \quad (1)$$

where $\overline{E}$ is the plane-strain modulus, defined as $E/(1-\nu^2)$, where E is the Young's modulus, and ν is the Poisson's ratio. The subscripts f and s refer to the top film and the bottom substrates, respectively. Equation 1 suggests that λ_0 is independent of the applied stress and strain. The amplitude of the wrinkle pattern, A_0, depends on the film thickness as well as the applied strain ε_0, and can be written as

$$A_0 = t \left(\frac{\varepsilon_0}{\varepsilon_c} - 1 \right)^{1/2} \quad (2)$$

where ε_c is the critical strain (the minimum strain needed for wrinkles to appear) given as

$$\varepsilon_c = -\frac{1}{4} \left(\frac{3\overline{E}_s}{\overline{E}_f} \right)^{2/3} \quad (3)$$

In many circumstances the bilayer system can be in a state of uniaxial or biaxial compression due to change in surrounding temperature or humidity. In order for the top layer to buckle, two conditions must be satisfied. First, considering only the top layer, it must develop in-plane compressive stress, and the magnitude of the stress must be above the critical threshold for buckling. Second, because the thin hard layer is confined by the bottom substrate, the latter must be compliant enough to allow out-of-plane deformation to accommodate the deformation of the top layer. A wide variety of hard films on soft elastomeric substrates have been studied. Here we focus on two common strategies to create wrinkles.

One simple approach is to deposit a hard thin layer (e.g., Au and Si) on top of a soft expanded substrate. For example, Bowden et al. fabricated wrinkles by depositing a thin Au layer on a thermally expanded PDMS film bonded to a glass slide, followed by cooling the substrate to the room temperature.[2] Because the PDMS film was confined on the substrate, only the top surface expanded during heating. Upon coating Au and cooling, the PDMS film shrank, generating a compressive stress to the top Au layer for wrinkling. If the sample was heated again the wrinkle pattern disappeared and reappeared upon cooling. The wrinkle pattern was very similar to those formed in the wrinkling of skin sheets in sandwich structures[64] but different from the waves in buckling-driven film delamination[65] because the metal films remain attached to the PDMS substrate.

This approach offers a sharp boundary between the hard thin coating and the soft substrate. One can precisely control the modulus and thickness of the thin film, thus, the wrinkle wavelength and amplitude. However, because the thin film is not covalently bonded to the soft substrate, it tends to delaminate from the substrate under a large strain, therefore, limiting the applicable strain level (typically < 10%) and miniaturization of the wrinkle size (typically in the range of tens to hundreds of micrometers). To address this issue, many have explored creating an oxide layer directly on PDMS film either by oxygen plasma or UV ozonlysis (UVO). During the plasma treatment or UVO exposure, the top surface of the PDMS oxidizes and converts into a thin layer of glassy silicate, of which the thickness and Young's modulus, thus the wrinkle wavelength and amplitude, are dependent on the plasma or UVO power and exposure time. Since the thin layer and the bulk substrate are essentially from the same material, potential delamination under a large strain is avoided. However, it also raises the complexity to model such bilayer system because there is no clear boundary between the oxidized layer and the underlying bulk PDMS to characterize exact thickness and modulus of the thin oxide layer.

While most wrinkle structures are formed by the heat-induced-strain method, which expands the PDMS substrate isotropically and simultaneously, we focus on creating wrinkles by mechanical stretching the PDMS film sequentially, followed by oxidation and strain release (**Figure 2**).[57] The use of mechanical force allows us to independently control the amount and timing of strain applied to the PDMS substrate on both planar directions (either simultaneously or sequentially). This added controllability in contrast to the heat-induced-strain method appears critical to maneuver the pattern formation and transition in real time.

2.2. 1D Ripple Patterns

As seen in Figure 2, a square-shaped PDMS strip (30 mm × 30 mm) was clamped (Figure 2a) and stretched (Figure 2b) in both planar directions sequentially. The strain in the first direction (Y) was fixed at a specific value, 20% (25 mm → 30 mm),

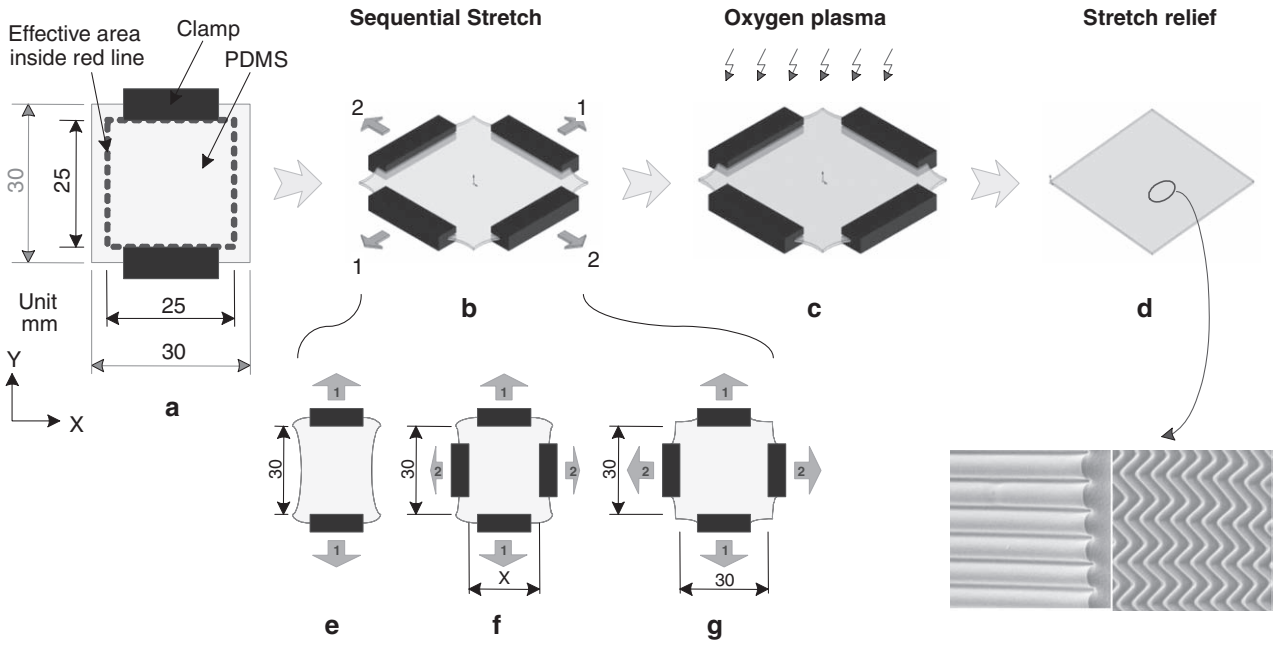

Figure 2. Schematic illustration of the fabrication process to generate wrinkle patterns (a–d) by sequential stretching of PDMS films at various mechanical stretch settings (e–g) used in (b). Inset in (d): SEM images of 1D ripples and 2D herringbone structured under either uniaxial or biaxial strain by sequential stretching/releasing, respectively.

and the strain in the second direction (X) was varied with a relative strain ratio ($\Delta X/\Delta Y$) ranging from 0 to 1 (Figure 2e–g) until reaching equal strain as in the first direction. The stretched sample was then treated with oxygen plasma (Figure 2c), followed by release in the reverse order (X first then Y) to generate uniform wrinkle patterns (Figure 2d).

When the sample was stretched/released in only one direction (Y) (Figure 2e), sinusoidal wavy ripple patterns were formed immediately once the compression spring force of substrate passed the critical buckling force (**Figure 3a**), and the wrinkle wavelength/amplitude agreed qualitatively with the estimation using Equations 1 and 2 (**Figure 4**), that is, the wavelength of ripples increased with increasing oxidation time due to increasing thickness and/or Young's modulus of the oxide film.[57] Further release did not change the shape of pattern, and most of the released strain deformation contributed to the increase of wrinkle amplitude as predicted by nonlinear theory.[51] When exposed to UVO for 30 to 60 min, a PDMS bilayer with wrinkle wavelength ranging from 15 to 30 μm was obtained.[14] Under O_2 plasma treatment (power 100–200 W) for 1 to 4 min, the wrinkle wavelength could be tuned between 250 nm and 10 μm.[14,57]

Since our experiments involve large deformation (up to 60% strain), which falls out of locally linearized domain, it is questionable whether Equation 1 can be applicable to our system, where the shear force should be taken into account[64] but was ignored in Equation 1. Equation 1 predicts that the wavelength should be independent of the applied strain level, and the amplitude should increase to accommodate the release strain. Instead, we observed that wrinkle wavelength decreased slightly with increasing pre-strain (Figure 4a),[57] suggesting that a denser packing of wrinkles was needed to accommodate larger strain. From the log–log plot shown in Figure 4b we found that the final wrinkle wavelength, at a much larger pre-strain (20%–60%), was linearly proportional to the oxygen plasma time with a slope of 0.25–0.27 instead of 1/3 as expected from Equation 1.

Recently, others also found that the wrinkle wavelength was not completely independent of the applied strain. Jiang et al.[66] developed a new a buckling theory that accounts for finite and large deformations and geometrical nonlinearities to predict the wavelength and amplitude:

$$\lambda = \frac{\lambda_0}{(1+\varepsilon_0)(1+\xi)^{1/3}} = \frac{2\pi t}{(1+\varepsilon_0)(1+\xi)^{1/3}}\left(\frac{\overline{E}_f}{3\overline{E}_s}\right)^{1/3} \quad (4)$$

and

$$A = \frac{A_0}{\sqrt{(1+\varepsilon_0)}(1+\xi)^{1/3}} = \frac{t}{\sqrt{(1+\varepsilon_0)}(1+\xi)^{1/3}}\left(\frac{\varepsilon_0}{\varepsilon_c}-1\right)^{1/2} \quad (5)$$

where $\xi = 5\varepsilon_0(1+\varepsilon_0)/32$, and λ_0 and A_0 are small deformation approximation wavelength and amplitude, respectively, given by Equations 1 and 2. $\lambda_0/(1+\varepsilon_0)$ and $A_0/(1+\varepsilon_0)^{1/2}$ represent the change of wavelength and amplitude expected due to pre-strain based on simple accordion bellows mechanics; $1/(1+\xi)^{1/3}$, which depends only on pre-strain, derives from geometric nonlinearities (finite deformation) and nonlinear constitutive model. For a small pre-strain, the value of λ approaches λ_0, although it retains the same functional variation with ε_{0non} down to pre-strains arbitrarily close to ε_c.

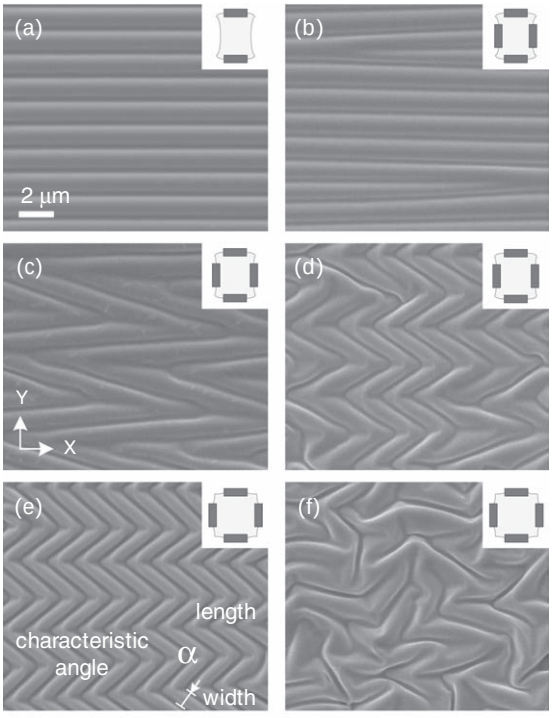

Figure 3. Most frequently observed SEM images of PDMS wrinkle patterns from 1D ripples in transit to 2D herringbones, which were released from different stretch conditions after oxygen plasma treatment. The scale bar in (a) is applicable to (a–f). The insets in (a–f) represent schematic stretch conditions. Equal stretches were applied in *Y* for all images (*Y* = 25 mm → 30 mm, 20% strain), with a) no stretch in the *X* direction (*X* shrinks from 25 to ~22 mm due to the Poisson effect), the same as shown in Figure 2e; b) *X* = 25 mm, stretching back to its original width of the effective area; c) *X* = 26.25 mm; d) *X* = 27.5 mm, the same as shown in Figure 1f; and e,f) *X* = 30 mm, where *X* and *Y* had the same strain level, the same as shown in Figure 1g. Strains applied and relieved in (b–e) were sequential, i.e., stretching in *Y* first and *X* second, while releasing in *X* first and *Y* second accordingly. f) Stretching and releasing simultaneously in both directions.

2.3. 2D Herringbone Structures and the Transition Between 1D Ripples and 2D Herringbones

When biaxial strain is applied to the PDMS bilayers, theories have suggested that it is possible to form various 2D wrinkle patterns, including checkerboards, labyrinths, and herringbone structures, by adjusting relative strain level between planar directions.[51,67] Simulations by Huang et al.[51] show that the wrinkles can evolve into stripes, labyrinths, or herringbones, depending on the anisotropy of the applied forces. Further, a checkerboard pattern is suggested when the strain level is slightly above the critical value, although experimentally such a pattern has not been observed. As the strain increases, segments zigzag to form labyrinths to relieve compression in all directions. The width of each zigzag segment agrees well with the wavelength of the stripe wrinkles. As the strain further increases, the segment width stays the same, but the segment length decreases. Interestingly, the simulation suggests that when anisotropy is introduced, that is, the strain applied in both planar directions becomes non-equivalent, wrinkles

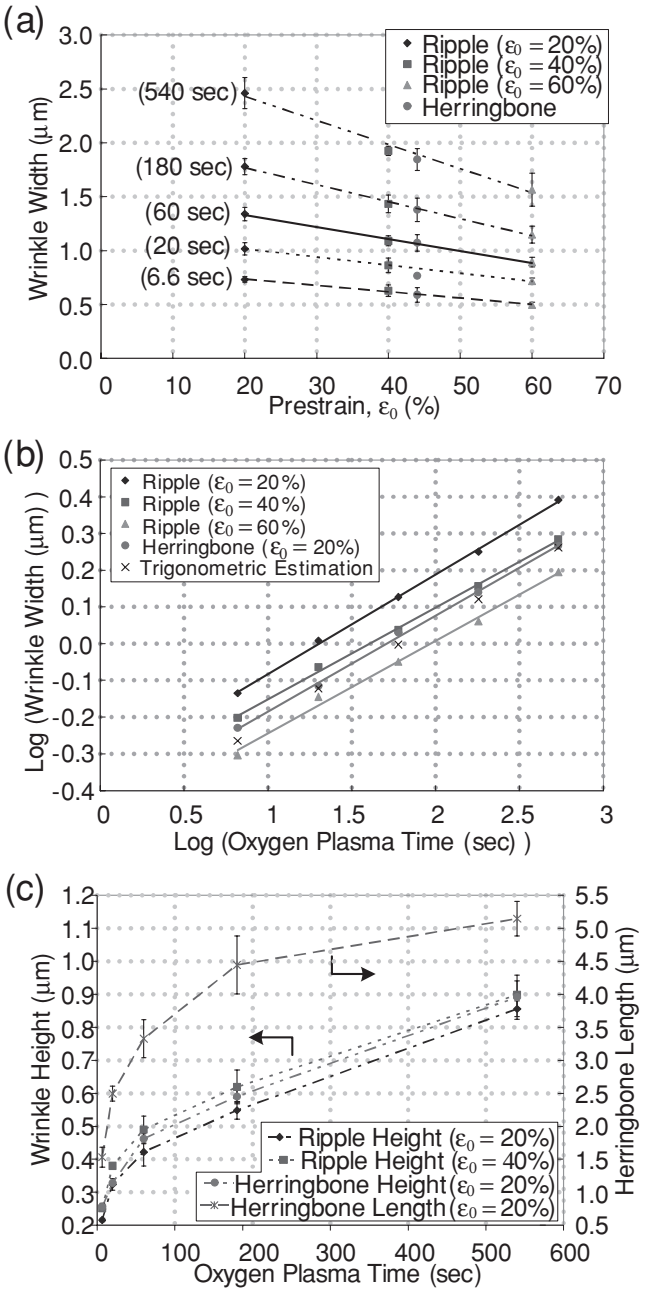

Figure 4. Characterization of ripple and herringbone structures formed under different conditions. The strains listed in the legends indicate the pre-strain (ε_0) applied before oxygen plasma treatment. The straight lines in (a) and (b) are linear fitting of the data. a) Final ripple width vs. release strain at different oxygen plasma times and stretch amounts. b) Log–log plot of final ripple and herringbone widths vs. oxygen plasma time. c) Final ripple and herringbone amplitude (left *Y* axis) and herringbone length (right *Y* axis) vs. oxygen plasma time. Reproduced with permission.[57] Copyright 2007, American Institute of Physics.

begin to have some directional preference and a perfect array of herringbones forms with obtuse elbow angles. As anisotropy increases, stripes form. Experimentally, however, few have shown highly ordered zigzag herringbone structures, nor demonstrated tuning between 1D ripples and 2D wrinkle structures

since most wrinkle patterns are obtained by heat-induced-wrinkling, which expands the PDMS equally and simultaneously.

In our system,[57] when the mechanical stretch was subsequently applied to the second direction (*X*) before oxidization process (Figure 2f and 2g), the final released wrinkle pattern was found gradually transiting itself from 1D ripples into various 2D patterns, from ripples with bifurcation (Figure 3b) to "truncated" ripples with bifurcation (zigzag) (Figure 3c) to a more symmetrical zigzag herringbone structure (Figure 3d), when the amount of stretch in the *X* direction was increased. When *X* was further increased to 30 mm reaching the same strain level as in *Y*, a highly ordered zigzag herringbone pattern was formed. As shown in Figure 3e, the edges of zigzags are parallel to each other and geometrical parameters (lengths, widths, and height) of zigzags are uniform with very small deviations. In contrast, a much disordered zigzag herringbone pattern was observed (Figure 3f) if the stretches in both *X* and *Y* directions were applied and released simultaneously, which is typically observed in heat-induced wrinkling patterns. To further elucidate the mechanism of pattern formation and transition, a series of in situ studies were performed under the optical microscope (**Figure 5a–j**). When released in one direction (*X*, Figure 5a–e), 1D ripples appeared (Figure 5b) with its width decreased slightly and gradually while continuing release the stretch (Figure 5c–e). When the stretch started to release in the *Y* direction as well (Figure 5l), the ripple became distorted and bifurcated (Figure 5f), then zigzag bending occurred on the original ripple pattern with a characteristic angle, α (see definition in Figure 3e), which propagated across the whole ripple columns as the release proceeded (Figure 5g–5i). When the stretch was fully released, the 1D ripple columns were completely bent into a highly ordered zigzag herringbone structure (Figure 5j). The result agrees well with the scanning electron microscopy (SEM) images seen in Figure 3 and with theory.[51] During the second release (Figure 5f–j), the width of the ripple remained unchanged, which further supports the concept of bending the ripple columns instead of reformatting the whole pattern to generate the final herringbone structures. In contrast, an irregular herringbone pattern was formed spontaneously in the case of simultaneous stretch/release (Figure 5m–r). The width of the herringbone continued to decrease with the increase of the wrinkle density while releasing the sample (Figure 5o–q) until the pre-strain was completely relieved in both directions (Figure 5r). This transition can be reversed when reapplying the stretch to the sample. The key to generate a highly ordered zigzag herringbone wrinkle pattern lies in the strategy of sequential release of the applied strain, which provides a well-controlled energy release path to achieve minimum elastic energy state. When the stretch is released in the second *Y* direction, the sample surface subjected to this new *Y*-direction buckling force is no longer a 2D flat plane but an array of ripple-shaped columns, which is in principle different from buckling a flat 2D surface in biaxial directions simultaneously. Thus, this orientation-regulating mechanism by generating ripple structure first guarantees the alignment of zigzag pattern directions after the second release. Further release did not change the shape of pattern, and most of released strain deformation contributed directly to the increase of wrinkle amplitude as suggested by recent nonlinear theories.[51]

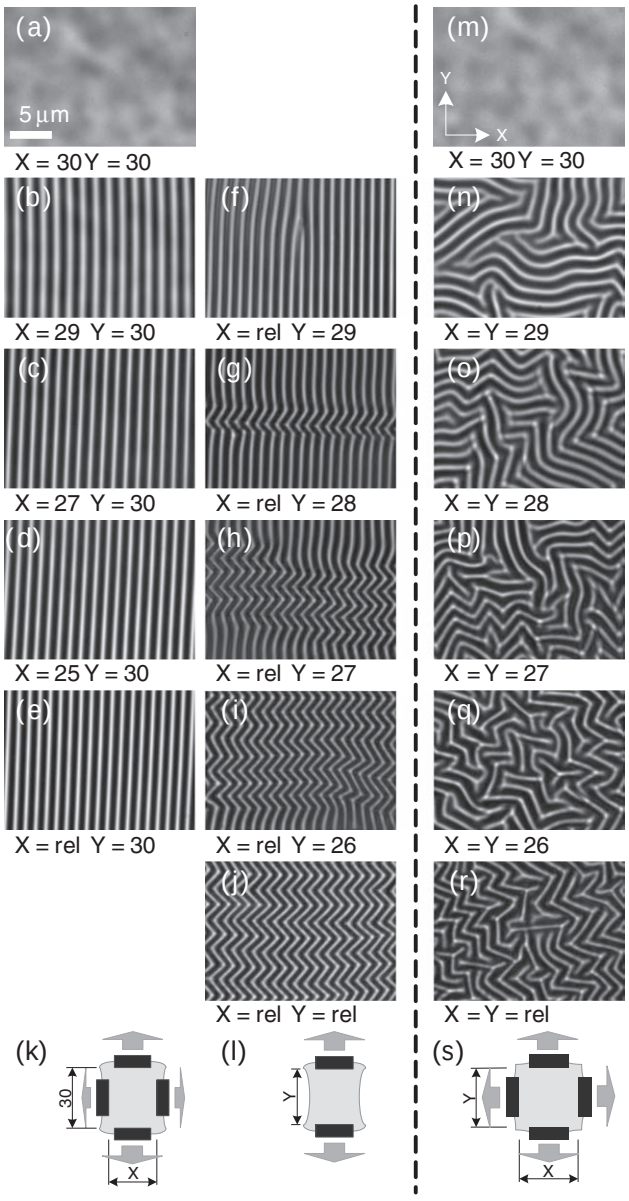

Figure 5. Two sets of sequential optical microscope images of two equally stretched PDMS samples (20% strain, from 25 to 30 mm on both edges) subjected to two different releasing processes, sequentially (a–j) and simultaneously (m–r), respectively, and their corresponding illustrative sketches (k–l) and (s), accordingly. The scale bar in (a) is applicable to all images. Reproduced with permission.[57] Copyright 2007, American Institute of Physics.

3. Swelling-Induced Surface Patterns in Hydrogels with Depth-Wise Crosslinkin Gradient

An alternative way of generating surface wrinkling patterns is by swelling a thin film of a confined elastoplastic polymer or hydrogel with a preferred solvent or monomer solution.[1,10,15,42,54,55,68] As seen in **Figure 6**, when the solvent swells the film, the surface area of the top of the film tends to increase while the bottom area, which is confined by the underlying rigid substrate, remains unchanged, therefore, generating an

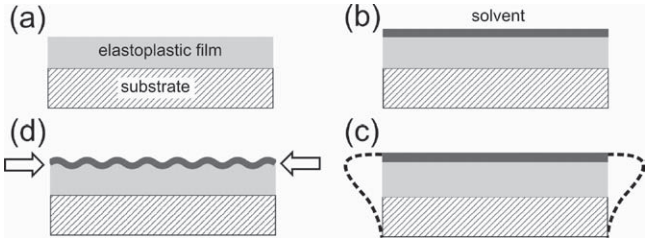

Figure 6. Schematics of swelling-induced wrinkling process. a) A thin film of an elastoplastic polymer is coated on a hard substrate. b) The elastoplastic film is swollen by a solvent. c) Upon swelling, since the bottom of the film is in confined on the rigid substrate, only top of the film can expand, resulting in a build-up of a compressive strain on film surface. d) Due to the compressive strain, the top surface of the film buckles, leading to wrinkle formation.

anisotropic osmotic pressure along the film thickness. When the osmotic pressure is greater than the critical value, the net compressive stress forces the outer surface to buckle, resulting in the formation of surface patterns.

Almost two decades ago, Tanaka et al. first reported on swelling-induced surface patterns in ionized acrylamide hydrogels constrained on a flat substrate.[1] The anisotropic osmotic pressure increases with time as the gel swells, leading to the evolution of surface patterns, here, creases, as a function of the osmotic pressure within the gel. Since this observation, many have attempted to manipulate the surface pattern formation in various hydrogels both experimentally and theoretically.[24,44–46,49,50,69] We note that most of the patterns formed are due to creasing instability instead of smooth surface wrinkling. For example, Trujillo et al. have shown crease formation when swelling poly(acrylamide-*co*-sodium acrylate) hydrogels cast on a coverslip.[24] Following polymerization the surface-attached gel is transferred to a phosphate-buffered saline (PBS) swelling solution until reaching equilibrium. The unidirectional swelling of a surface-attached gel resulted in a biaxial compressive stress, which was partially relieved by localized creasing of the gel surface. While both creasing and wrinkling instabilities originate from buckling of a material's outer surface to relieve compressive stress, critical conditions for creasing and wrinkling, and pattern characteristics are distinct. In the case of wrinkling, application of a relatively small compressive stress to a bilayer film system with a thin hard layer coated on a soft substrate or a gel under load or upon swelling by a solvent leads to the formation of low-aspect ratio sinusoidal features. Wrinkling instability is mainly driven by mismatch of the elastic modulus of the two layers and the resulting wrinkle pattern depends upon the thickness of the top layer and the ratio of the elastic modulus of the two layers. By controlling the direction of the applied stress, one can generate highly ordered, hierarchal, or completely random wrinkle patterns.[57,70] Creasing instability, on the other hand, occurs at a large compressive strain, even in a single homogeneous layer system, e.g., a highly swellable gel bonded on a rigid substrate or bending an elastic rod, resulting in sudden formation of sharp folds on the surface.[1,23,24,43,71–73] While different sets of critical strain (ε_c) for creasing have been reported, theory predicts $\varepsilon_c \approx 0.35$,[25] which agrees with some experimental values.[23,72] We note that theory assumes there is no solvent migration in the gel, thus resembling incompressible elastomers.

Chan et al. have demonstrated the wrinkle formation by swelling an elastomeric film, poly(*n*-butyl acrylate) (P*n*BA), with its monomer solution on a glass substrate.[15] Because the P*n*BA film is pinned to the rigid glass substrate, the lateral expansion of the polymer film is confined, leading to the formation of surface wrinkle patterns. After the brief swelling process, the wrinkled film was irradiated with ultraviolet (UV) light to stabilize the surface wrinkles. Later, the same group exploited diffusion-controlled surface wrinkling by swelling UVO treated PDMS films.[54] The UVO exposure produced a stiff oxide layer on PDMS outer surface region, which resists swelling by the organic solvent vapor, thus, the solvent vapor preferentially swelled the underlying PDMS film. The wrinkle morphologies were dictated by the location of buckle initiation and solvent diffusion kinetics. In a similar vein, Chung et al. produced highly ordered wrinkle patterns, both equilibrium and kinetically trapped, by swelling an UVO treated polystyrene (PS) thin film on a substrate.[21] The UVO exposure led to oxidation and crosslinking of the PS chains in the outer surface region, forming a hard skin on PS. When the film was placed in a closed chamber of supersaturated toluene vapor, which preferentially swelled the underlying non-crosslinked PS, a rich variety of surface wrinkles were observed when above a critical stress value, including flower-like patterns, spokes, targets, labyrinths, and dots, and the pattern morphology exhibited a clear dependence on the UVO exposure time. The characteristic wavelength of the patterns also increased with UVO exposure time. This is due to the fact that longer UVO exposure time generates thicker oxidized PS film leading to larger wrinkle wavelength as suggested by Equations 1 and 4.

In comparison to PDMS and other elastomers or elastoplastic polymers, there are a wide range of hydrogels with tunable chemistry and functionality, which will allow us to manipulate crosslinking density and gradient, and responsiveness to environmental stimuli (e.g., heat, light, electrical potential, chemicals, and biological agents). Therefore, hydrogel systems potentially could offer much richer materials properties to create a variety of surface patterns than the PDMS bilayer system. However, it remains elusive to create smooth wrinkle patterns from hydrogel films. Due to the large swelling ratio of hydrogels in water, and thus, large strain imposed to the film, most patterns formed from swelling-induced instability in hydrogels are creases. Furthermore, the hydrogel swelling is rather nonlinear, therefore, the imposed stress is always much greater than the critical value for buckling, making it difficult to control the long-range order.

Recently, we have generated a series of surface wrinkling patterns and observed their dynamic evolution, from highly ordered hexagonal pattern in transit to peanut shape, lamellar, and random worm-like structures, when swelling poly(hydroxyethyl methacrylate) (PHEMA) hydrogel films with modulus gradient and confined on a flat substrate (**Figure 7**).[42] The PHEMA films were prepared from a UV curable precursor solution composed of partially polymerized PHEMA, a photoinitiator, and a crosslinker (ethylene glycol dimethacrylate, EGDMA), which was spin-coated on to a substrate (metharcylate silane treated Si wafer or glass slide) (Figure 7a,b). It is well-known

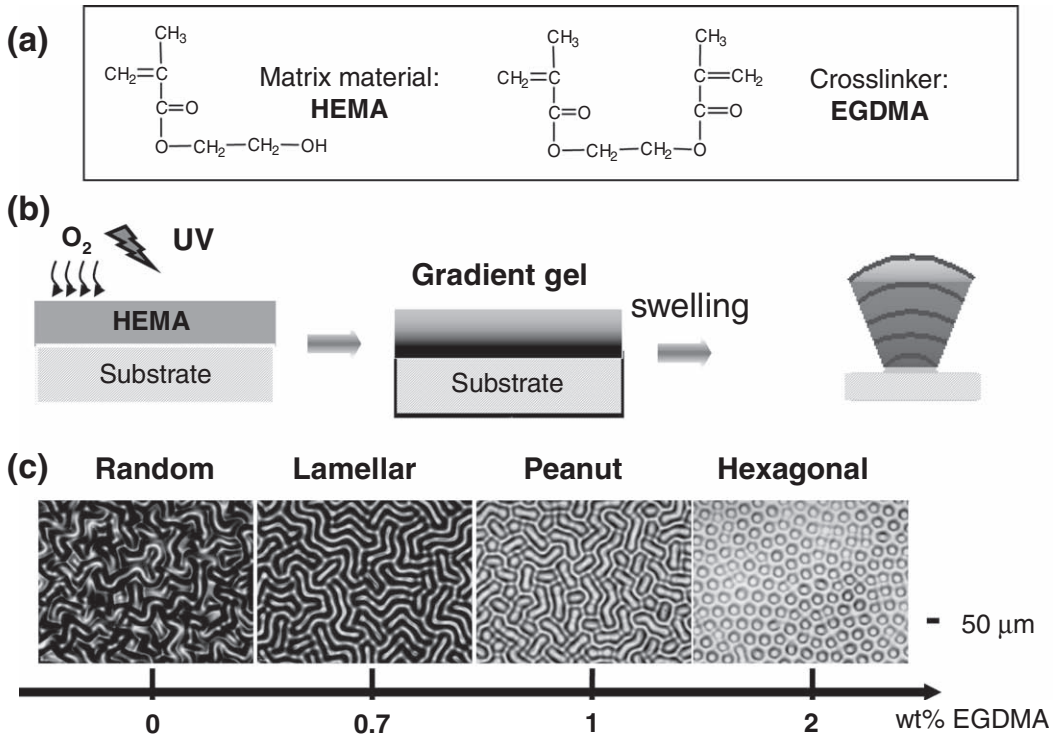

Figure 7. The dynamic evolution of a wide range of surface patterns, including a highly ordered hexagonal pattern in transit to peanut shape, lamellar, and random worm-like structures, in PHEMA hydrogel films with a modulus gradient through the film depth. a) Chemical structures of the monomer, HEMA, and crosslinker, EGDMA. b) Schematic illustration of the fabrication of PHEMA films with a modulus gradient and formation of wrinkling patterns upon swelling. c) Optical images of patterns on the surfaces of DI-water-swollen PHEMA films. The order of the patterns is determined by the concentration of crosslinker EGDMA.

that dissolved oxygen can consume radicals, hence, inhibiting photopolymerization and crosslinking of polymers until dissolved oxygen is depleted to a minimal level. For PHEMA films thicker than 20 μm, the consumed oxygen could not be replaced fast enough to limit crosslinking, and the amount of diffused oxygen gradually decreased along the film depth. By controlling film thickness and crosslinker concentration, and thus O_2 diffusion in the hydrogel film during the UV curing of PHEMA films, we created a modulus gradient with depth: the top surface (near air) had a lower crosslinking density and modulus, which gradually increased with film depth, and leveled off after reaching the critical depth for oxygen diffusion (Figure 7b and **Figure 8**). The crosslinking gradient profile with depth can be modulated by the concentrations of initiator and crosslinker EGDMA, precursor viscosity, exposure time and intensity, and film thickness.

When a droplet of water was placed on the gradient PHEMA film surface, four distinctive wrinkling patterns, including random worms, lamellae, peanuts, and long-range ordered hexagonal patterns, were formed spontaneously within the trace of the water droplet, depending on EGDMA concentration (Figure 7c). The gradient crosslinking density plays a critical role in the evolution of surface patterns and their ordering together with lateral confinement of the gel. No pattern was observed when swelling a uniformly crosslinked film nor when the EGDMA concentration was ≥ 4 wt%. In the latter case, the film was highly crosslinked throughout the film to resist

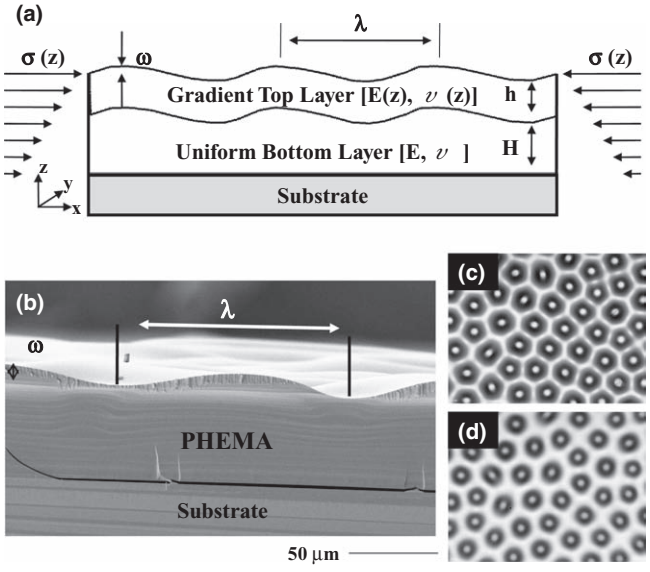

Figure 8. a) Schematic illustration of gradient hydrogel film, which is composed of two layers: bottom layer with uniform mechanical properties and a thinner top layer with gradient modulus due to oxygen inhibition during photocrosslinking. b) Cross-sectional SEM image of swollen PHEMA film with hexagonal order. Optical images of c) dry and d) swollen films, respectively. λ is the characteristic wavelength, υ is the Poisson's ratio, E is the Young's modulus, σ is the stress. Reproduced with permission.[42]

swelling by water, leading to an internal osmotic pressure below the threshold.

In a swollen gel, the instability is determined by the competing forces of osmotic pressure (P) and lateral confinement:[1]

$$P = \left(E_2^{1/2} \frac{kh}{3} - E_0^{1/2} \frac{1}{kh} \right)^2 + \frac{2}{3} (E_2 E_0)^{1/2} \quad (6)$$

The critical pressure for buckling (P_c) with a critical wavelength (λ_c) is

$$P_c = \frac{2}{3} (E_2 E_0)^{1/2}, k_c = \frac{2\pi}{\lambda_c} = \left(\frac{E_0}{E_2} \right)^{1/4} \frac{\sqrt{3}}{h} \quad (7)$$

which is roughly proportional to the average Young's modulus of a uniform gel ($P_c \approx E$) and independent of the film thickness (h), whereas λ_c is proportional to the film thickness and dependent on the modulus. For the gradient gels, the modulus of the film at the surface and bulk differs much so that E_2 is approximated as the effective modulus for the surface (E^*) and E_0 is approximated as bulk modulus of the bottom region (E). By plotting P vs. $(kh)^2$, we can observe the trend of the modulus gradient on pattern stability: the critical stress required to buckle films increases sharply with the increase of E/E^*, a steeper gradient in modulus when increasing EGDMA concentration.

In agreement with the prediction by Tanaka et al.,[1] we found that the wrinkle pattern ordering was nearly independent of the film thickness, whereas the characteristic wavelength (λ = 40–120 μm) increased linearly with film thickness (30–250 μm) and was dependent on the film's Young's modulus, E. We observed that the order and characteristic wavelength of the patterns formed in swollen states and dry conditions were nearly identical and remained stable during subsequent swelling, which could be attributed to the transition of PHEMA from a rubbery (swollen) to glassy (dry) state during drying, thus, locking the equilibrium pattern upon drying. We would like to point out that the wrinkle formation in this approach is different from the bilayer system, where a thin hard skin is coated on a soft elastomer sheet (see discussion in Section 2), and that by swelling of a homogeneous hydrogel film on a rigid substrate.[1,24] In the latter, creases are commonly formed and it is difficult to obtain perfectly hexagonal patterns due to the large swelling ratio such that the stress is always beyond the critical threshold. By manipulating the crosslinker concentration in the gradient gels, we are able to fine-tune the anisotropic osmotic pressure near the threshold, allowing for control of the long-range order and morphology of the final patterns.

4. Applications of Surface Wrinkling

Above we have discussed several methods to creating surface wrinkles in different materials. It will be intriguing to harness the wrinkle patterns for advanced technologies. Due to the periodic structure of wrinkles, they have been investigated for many applications, including diffraction gratings,[2,9] stretchable electronics,[7,8] cell adhesion and growth,[74] antifouling,[75] microcontact printing,[76] and maskless lithography.[77] Here we will present a few exemplary applications of PDMS wrinkle structures by taking advantage of their periodicity and tunable topography.

4.1. Tunable Adhesion

The ability to reversibly tune the adhesion of a material to another surface in a controlled fashion is highly desirable for many applications, including micro- and nanoelectronics, optoelectronics, biotechnology, and robotics. Generally, adhesion between any two surfaces is proportional to the effective contact area, surface chemistry, and compliance of the substrates.[78] Between two elastomeric sheets, Gent has investigated strength of adhesion vs. the rheology of the rubbery substrates.[79] He shows that the adhesion and tear strength of rubbery solids increases at higher tearing speed and lower temperature. Later, by kinetically control the adhesion to a flat PDMS stamp, Meitl et al. have demonstrated transfer printing a wide range of objects, including p–n junctions and photodiodes, silica microspheres, and grains of pollen.[76]

Because of the elastomeric nature of PDMS films, the topography of PDMS wrinkles can be reversibly tuned from a sinusoidal wavy shape to completely flattened, and we have explored the application as a tunable adhesive simply by mechanical stretching.[16] It has a set of advantages not offered by other techniques for regulation of adhesion, including real-time tunability, no requirement of specific surface chemistry, operability under ambient conditions, and relative ease of control. Adhesion of the tunable topographic wrinkles was measured by indenting a glass sphere, connected to a load cell, into the sample and then retracting. While the indenter was retracted, the maximum force supported by the indenter, the pull-off force, F_{ad}, gives the measure of the adhesion between the two surfaces. **Figure 9** shows the force displacement data from a series of experiments at different values of pre-strains. The measure of the strain was defined as ε_0 (pre-strain) – ε (release strain). It is clear that the adhesion reduces systematically and significantly with the increase in ε, which is accompanied by an increase in the wrinkle amplitude. For 0% strain, where the ripple sample is almost flat, the adhesion is at maximum, close to that of a flat (control) sample. On such rippled surface, we have performed a "pick and release" experiment to illustrate the real-time tunability (**Figure 10**). Without stretch, the PDMS film with surface wrinkle patterns shows very little adhesion force that could hardly lift the glass bead. When the film is stretched and flattened, the glass ball can be easily lifted until the gravity exceeds the adhesive force between glass ball and PDMS film. When releasing the flattened film, the surface roughness is regenerated, thus decreasing the adhesion force. The pick and release process can be controlled reversibly and repeatably in real time.

Theoretical modeling of the tunable adhesion shows that in the limit of small amplitude can be analyzed by extending Johnson–Kendall–Roberts (JKR) theory to account for energy released during rippling.[16] At the interemediate amplitude, we have developed a new model that accounts for partial contact between the indenter and rippled surface. This tunable

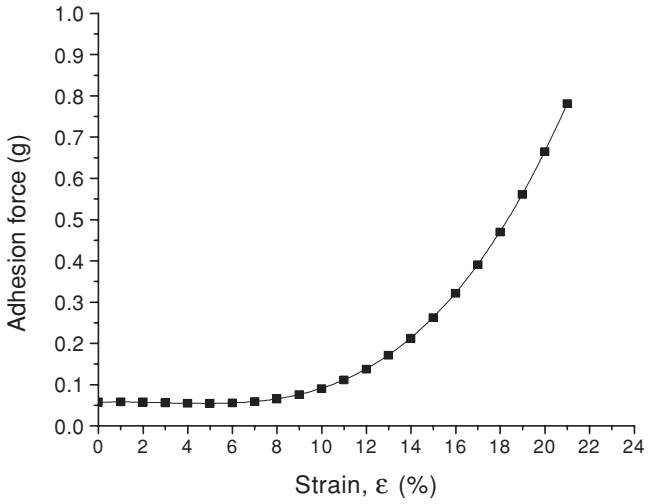

Figure 9. Adhesion (pull-off force) vs. strain level on rippled PDMS (pre-strain, $\varepsilon_0 = 22.4\%$).

adhesion using PDMS wrinkles will offer valuable insights for the design of tunable friction and wetting behaviors based on surface topography.

4.2. Tunable Wetting

On the basis of the same tuning mechanism, we demonstrate the dynamic switching of wetting behaviors and flow resistance on the rippled PDMS bilayer film, as well as to elucidate the wetting transitions between different states. Surface wetting behavior is strongly dependent on both surface chemistry (i.e., surface energy) and surface topography (i.e., physical roughness). Many groups have attempted dynamic tuning of surface wettability from superhydrophobic to hydrophilic by using responsive polymer brushes,[80,81] varying surface roughness,[82–84] and applying an external field (e.g., electrowetting).[85,86] However, questions remain as how microscopic and nanoscopic roughness (surface chemistry, morphology, and geometry) contribute to the wettability and transition, and whether it is possible to reversibly switch between different (non)wetting states.

While the adhesion on rippled PDMS can be tuned in real-time as a function of strain level, the water on these microscale ripples tends to be pinned, therefore, constraining the mobility of droplets to achieve both self-cleaning and tunable dry adhesion as shown in gecko's foot hairs.[87] To promote the surface wetting into Cassie-Baxter's state,[88] that is, a composite non-wetting surface with low flow resistance, we integrated nanoparticles into the rippled system to generate dual-scale roughness, which was suggested critical to the observed superhydrophobicity in many aquatic plants[89] and animal hairs.[87]

The fabrication of dual-scale PDMS ripple surface is illustrated in **Figure 11**. After stretching (Figure 11b) and oxygen plasma treatment (Figure 11c), the PDMS bilayer film is dip-coated with silica nanoparticles (Figure 11d) for nanoscale roughness, which is subsequently hydrophobilized by (heptadecafluoro-1,1,2,2-tetrahydrodecyl)trichlorosilane (Figure 11e). Finally, the dual-structured surface is obtained after releasing the initial strain (Figure 11f). When the sample is stretched back to the initial strain (Figure 11g), only the nanoscale roughness provided by nanoparticle film remains. Study of water contact angles on various surfaces (**Figure 12**) suggests wetting transition from a Wenzel regime (a wetting state, on both microscale-rippled PDMS and nanoparticle film) into a Cassie-Baxter regime (a non-wetting state, on the dual-rough surface). More strikingly, the sliding angle of the dual-scale rough surface is reduced at least three times (from ~58° on nanoparticle film to ~16°) in comparison to the surfaces with single-scale roughness, simply by mechanically stretch the PDMS films.

4.3. Tunable Open-Channel Microfluidics

Another application related to the 1D wrinkle topography is open-channel microfluidics.[14] When the dimension of microfluidic channels is reduced to several hundreds of micrometers, the surface forces become dominant. However, the small channel size also poses one major challenge in application of conventional microfluidic devices, which is that where a liquid flows in a closed solid matrix under pressure the channel can be easily clogged. In contrast, open microfluidics, where a liquid has an accessible liquid–air interface, are relatively easy to fabricate and more importantly, they can be cleaned and reused conveniently if channels are clogged. It has been shown that in open microfluidic channels the wetting morphologies and the liquid transport dynamics are dependent on the groove geometry and the wettability of the substrate.[14] Since the surface topography of PDMS wrinkles can be reversibly tuned

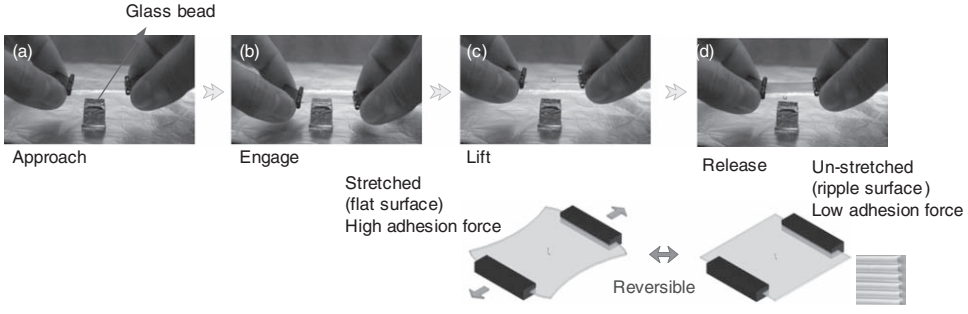

Figure 10. Sequential images of using rippled PDMS film to pickup and release a glass bead.

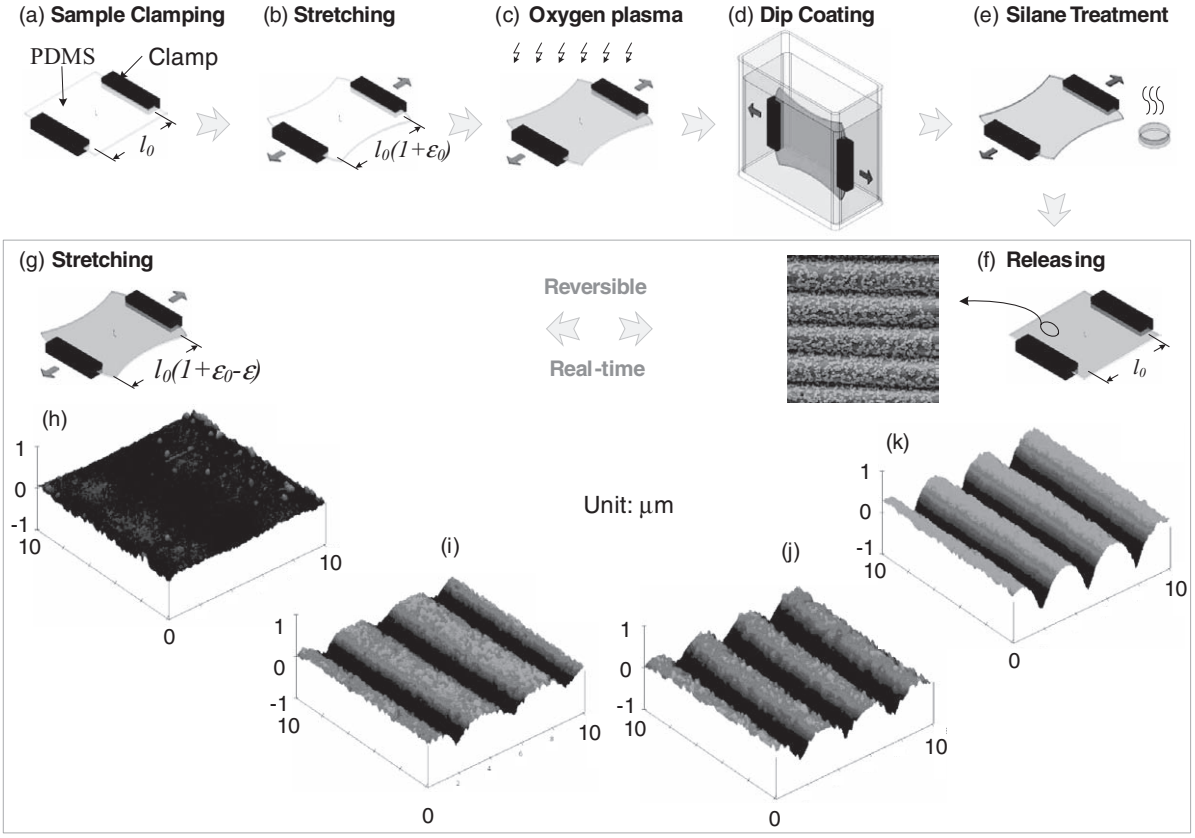

Figure 11. Schematic illustration of fabrication of a PDMS film with dual-scale roughness (a–f) and real-time, reversible tunability of its surface topography by mechanical strain (f–k). a) Clamping a PDMS film. b) Stretching the PDMS film to a designated initial strain value. c) Oxygen plasma treatment. d) Dip-coating the stretched sample. e) Silane Treatment. f) Releasing stretch of the sample and spontaneous formation of microscale ripple patterns. g) Stretching back the sample to the initial strain value. The ripple patterns disappear and only nano-scale roughness remains. h–k) Atomic force microscopy (AFM) images of the samples at different stretch conditions. Reproduced with permission.[13] Copyright 2009, The Royal Society of Chemistry.

simply by mechanical stretching, and their surface chemistry can be varied by coating self-assembled monolayers (SAMs) or polymer brushes, the sinusoidal PDMS wrinkles could offer additional degrees of freedom to manipulate both the geometry (wavelength and amplitude) and chemistry, thus wettability and liquid transport.

When a drop of a liquid is placed on a 1D wrinkled substrate it forms an asymmetric shape: the droplet forms a Young's contact angle in a direction parallel to the grooves, where there is no energy barrier for the moving contact line; whereas in the other direction perpendicular to the grooves, there is larger energy barrier for the moving contact line, thus, the three phase contact line of the liquid gets pinned, resulting in a much larger contact angle. **Figure 13a** shows the anisotropic wettability of a glycerin droplet on a 1D wrinkled substrate, which has a Young's contact angle, $\theta = 46°$. When the wrinkle surface is stretched and completely flattened, the liquid forms a circular drop (Figure 13b). This wetting anisotropy, for a fixed Young's contact angle (or surface chemistry), increases when the grooves become deeper. On substrates with a Young's contact angle smaller than 90° and deep grooves (aspect ratio ≥ 0.3), liquids form filament-like morphology. As the applied strain is released, the amplitude of the wrinkle grooves increases. Beyond a threshold amplitude (corresponding to the threshold compressive strain), the value depends on the surface wettability, the liquid starts imbibing the grooves (Figure 13c–e). If the strain is further released, the length of the liquid filament also increases (Figure 13e). For fully relaxed wrinkle film, the liquid fills the entire length of the grooves (Figure 13d). The study of the dynamics of the liquid imbibition of grooves suggests a square-law dependence between the length of the liquid filament and time, which obeys Washburn's law.

4.4. Strain-Responsive Microlens Arrays

Microlenses with variable focal length are of interest to increase the efficiency of the light detection, recording, imaging, and coupling. However, the attainable range of tunability in most technological microlenses is rather limited once they are fabricated. A wide variety of tuning mechanisms have been reported, including responsive hydrogels,[90] electrowetting,[91] liquid pressure to deform an elastomeric membrane,[92] liquid crystal microlens arrays,[93] and integrated microfluidic channels,[94] to tune lens shape, refractive index, and the surrounding medium. Nevertheless, most of these microlens arrays are multicomponent

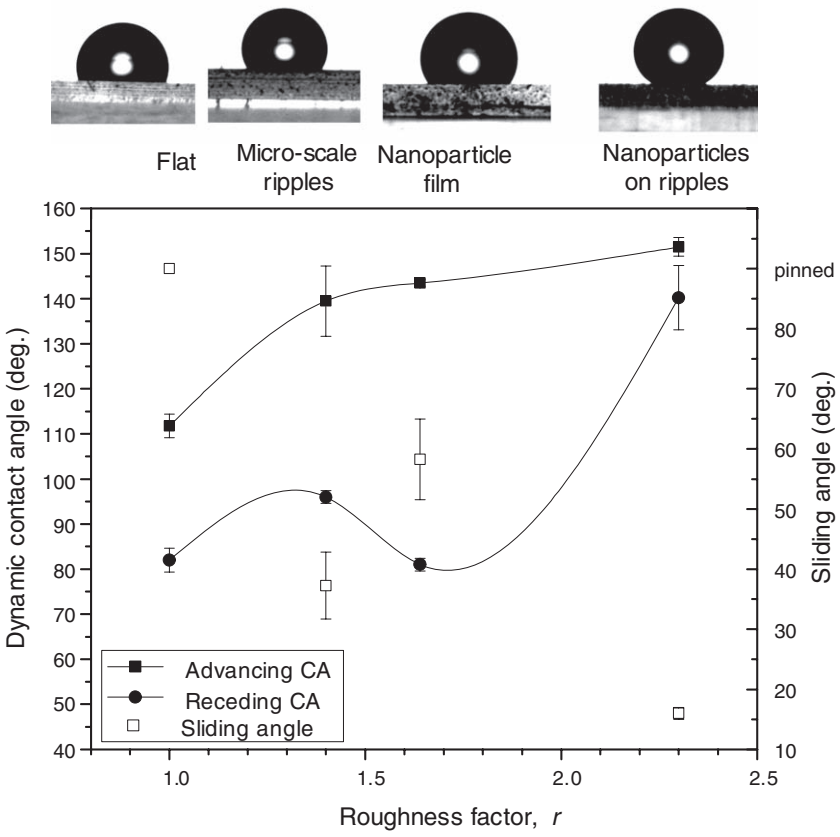

Figure 12. Dynamic contact angles and sliding angles on various rough surfaces. For both rippled surfaces (microscale ripples and nanoparticles on microscale ripples), the contact angles were measured in the direction along with ripple grooves. Optical images: static contact angles of 6 μL water droplets on the various surfaces. Lines are used to guide the eyes.

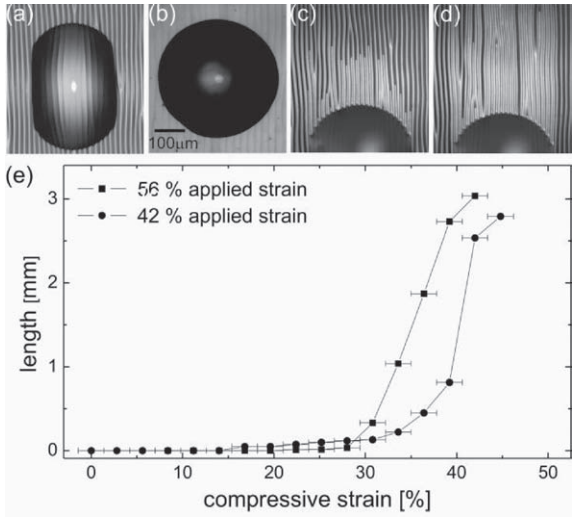

Figure 13. Open-channel microfluidics using 1D rippled PDMS film. a) A glycerin drop showing anisotropic wettability on 1D ripples. b) If the wrinkles are stretched to completely flattened, the drop becomes isotropic. c) As the stretching is released, the wrinkle amplitude increases, and beyond the critical strain, the liquid starts imbibing the wrinkle grooves. d) On fully released wrinkles, the liquid fills the whole length of the grooves. e) Plot of the length of the liquid filaments as a function of the compressive strain for two different samples with applied strains of 42% and 56%, respectively.

systems, and some systems cannot change the focal length continuously in real-time. By taking advantage of the wrinkling effect in a bilayer PDMS film, we have fabricate a single-component, strain-responsive, microlens array (both concave and convex) with real time tunable focus (**Figure 14**).[11] The concave lens array was fabricated by patterning a thin oxide layer on a biaxially pre-stretched PDMS through shadow mask, followed by confined buckling upon release of the pre-strain. The convex microlens array is then replica-molded from the concave lenses in PDMS. In experiments, a square sheet ($25 \times 25 \times 0.5$ mm^3) of thin PDMS film was stretched to 20% strain in both planar directions simultaneously (Figure 14a). One side of the PDMS sheet was masked by a transmission electron microscopy (TEM) copper grid with hexagonally packed hole array, followed by UVO exposure for 30 min. The mask was then removed and the strain was released in both planar directions simultaneously, resulting in a concave microlens array. Previously, a similar strategy was used to create a microlens array by swelling a patterned oxide/PDMS bilayer structure with acrylate monomers, followed by polymerization.[10] However, such formed acrylate lenses are rigid and not tunable. In contrast, the lens shape in our PDMS lenses can be reversibly tuned simply by applying a mechanical strain.

Because the concave and convex lenses are formed differently, they show different tunable range of focal length in response to the applied strain (Figure 14b–c): a large focal length change is observed from the concave microlens array whereas that from the convex microlens array is much smaller. Since the concave microlenses are formed under the buckling force when the pre-strain ε_0 is released after formation of the oxide layer, they could be completely flattened when the applied strain becomes equal to the pre-strain, therefore offering large tunability of the focal length. In the case of convex microlenses, which are replicated from the concave microlens, there is no buckling involved in lens formation. When a convex microlens is stretched, the lens volume remains constant due to the Poisson's ratio of PDMS ($\nu \approx 0.5$) such that the lens cannot be completely flattened, resulting in a considerably smaller focal length tunability.

5. Conclusion and Perspectives

Mechanical instabilities in soft materials, specially wrinkling, have led to the formation of unique surface patterns for a wide range of applications that are related to surface topography and its dynamic tuning. In order to understand and manipulate the surface wrinkling patterns, we have investigated two types of systems, including 1) mechanically stretching oxide/PDMS

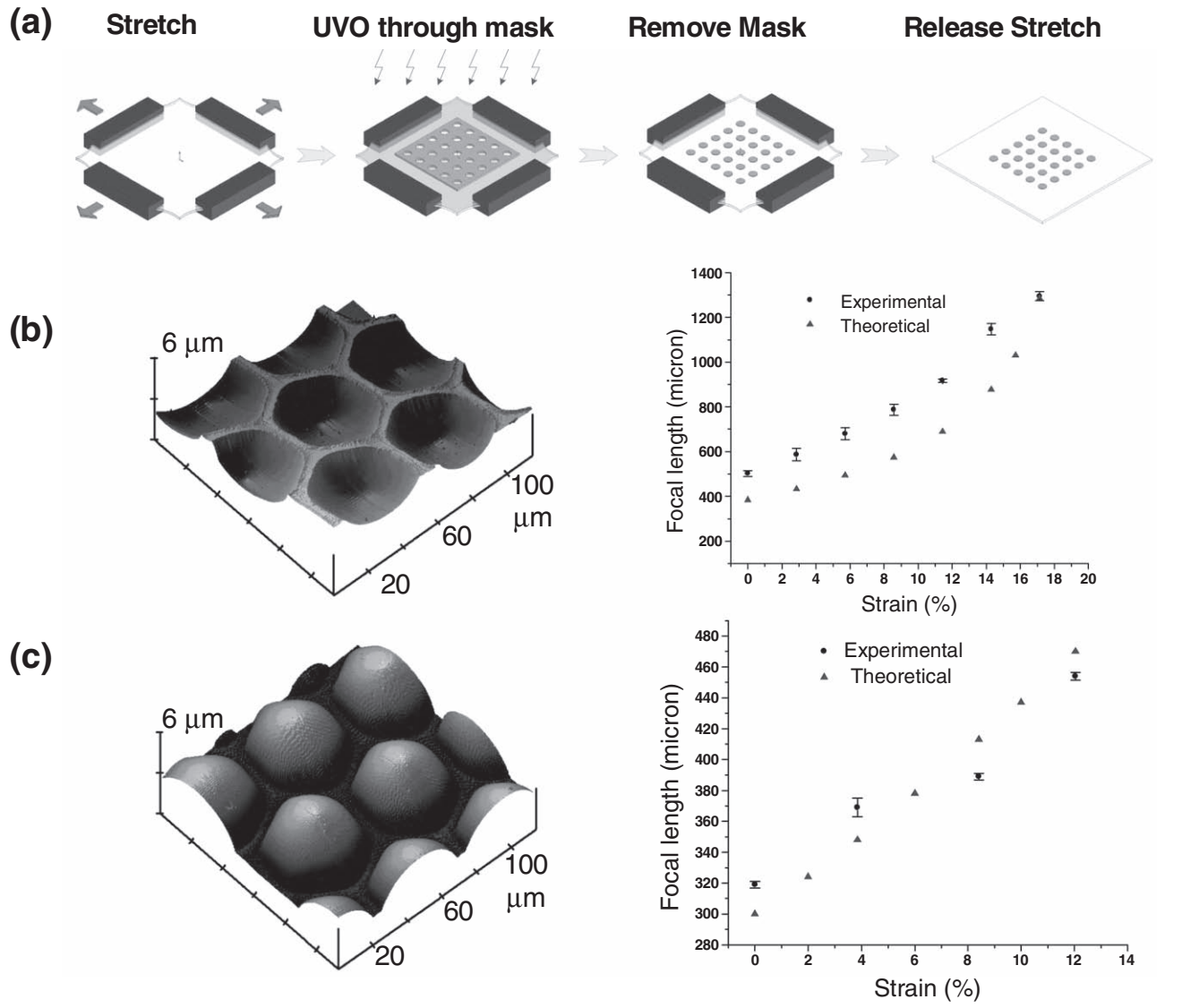

Figure 14. Strain-responsive microlens arrays. a) Schematic illustration of the fabrication procedure of concave microlens array. b) AFM image of concave microlens array and the corresponding focal length vs. applied strain. c) AFM image of convex microlens array and the corresponding focal length vs. applied strain.

bilayers and 2) swelling-induced wrinkling on hydrogel films confined on a rigid substrate with a modulus gradient along film thickness, and studied the respective wrinkling mechanism and transition between different wrinkle patterns. We have suggested approaches to control the wrinkle pattern order and characteristic wavelength.

We also demonstrate that the tunable wrinkled PDMS surfaces promise a wide range of novel applications, including tunable adhesion, wetting, microfluidics, and microlens arrays. We currently explore diffusion-controlled, kinetically trapped wrinkle patterns in different materials systems. We are also investigating their uses in biological applications, such as cell alignment and patterning. We envision that this review will shed light on design of complex structures, for example, by confining the wrinkle formation in patterned regions, wrinkling in non-homogeneous elastomers or gels, and assembly of functional nanoparticles (e.g., Au, Ag, and quantum dots), and their dynamic tuning. The new studies in elastic instabilities will be valuable for the technological advancement in micro- and nanofluidic applications, electronics and optoelectronics, as well as for driving new paradigms in biotechnology and soft robotics.

Acknowledgements

This work is supported in part by the National Science Foundation (NSF) CAREER Grant # DMR-0548070, and NSF/MRSEC Grant # DMR-0520020. We are grateful to Prof. Anand Jagota of Lehigh University, Prof. Chung-Yuen Hui of Cornell University for helpful discussion and collaboration on tunable adhesion.

Received: January 7, 2010
Published online: July 29, 2010

[1] T. Tanaka, S. T. Sun, Y. Hirokawa, S. Katayama, J. Kucera, Y. Hirose, T. Amiya, *Nature* **1987**, *325*, 796.
[2] N. Bowden, S. Brittain, A. G. Evans, J. W. Hutchinson, G. M. Whitesides, *Nature* **1998**, *393*, 146.
[3] B. A. Grzybowski, K. J. M. Bishop, C. J. Campbell, M. Fialkowski, S. K. Smoukov, *Soft Matter* **2005**, *1*, 114.
[4] C. Jiang, S. Singamaneni, E. Merrick, V. V. Tsukruk, *Nano Lett.* **2006**, *6*, 2254.
[5] Y. Klein, E. Efrati, E. Sharon, *Science* **2007**, *315*, 1116.
[6] Y. Zhang, E. A. Matsumoto, A. Peter, P. C. Lin, R. D. Kamien, S. Yang, *Nano Lett.* **2008**, *8*, 1192.
[7] S. Wagner, S. P. Lacour, J. Jones, P. H. I. Hsu, J. C. Sturm, T. Li, Z. G. Suo, *Phys. E* **2004**, *25*, 326.
[8] D. Y. Khang, H. Q. Jiang, Y. Huang, J. A. Rogers, *Science* **2006**, *311*, 208.
[9] C. Harrison, C. M. Stafford, W. H. Zhang, A. Karim, *Appl. Phys. Lett.* **2004**, *85*, 4016.
[10] E. P. Chan, A. J. Crosby, *Adv. Mater.* **2006**, *18*, 3238.
[11] D. Chandra, S. Yang, P. Lin, *Appl. Phys. Lett.* **2007**, *91*, 251912.
[12] J. Y. Chung, J. P. Youngblood, C. M. Stafford, *Soft Matter* **2007**, *3*, 1163.
[13] P. C. Lin, S. Yang, *Soft Matter* **2009**, *5*, 1011.
[14] K. Khare, J. Zhou, S. Yang, *Langmuir* **2009**, *25*, 12794.
[15] E. P. Chan, E. J. Smith, R. C. Hayward, A. J. Crosby, *Adv. Mater.* **2008**, *20*, 711.
[16] P. C. Lin, S. Vajpayee, A. Jagota, C. Y. Hui, S. Yang, *Soft Matter* **2008**, *4*, 1830.
[17] X. L. Zhu, Y. Zhang, D. Chandra, S.-C. Cheng, J. M. Kikkawa, S. Yang, *Appl. Phys. Lett.* **2008**, *93*, 161911.
[18] J.-H. Jang, C. Y. Koh, K. Bertoldi, M. C. Boyce, E. L. Thomas, *Nano Lett.* **2009**, *9*, 2113.
[19] C. M. Stafford, C. Harrison, K. L. Beers, A. Karim, E. J. Amis, M. R. Vanlandingham, H. C. Kim, W. Volksen, R. D. Miller, E. E. Simonyi, *Nat. Mater.* **2004**, *3*, 545.
[20] J. Huang, M. Juszkiewicz, W. H. de Jeu, E. Cerda, T. Emrick, N. Menon, T. P. Russell, *Science* **2007**, *317*, 650.
[21] J. Y. Chung, T. Q. Chastek, M. J. Fasolka, H. W. Ro, C. M. Stafford, *ACS Nano* **2009**, *3*, 844.
[22] J. Genzer, J. Groenewold, *Soft Matter* **2006**, *2*, 310.
[23] A. N. Gent, I. S. Cho, *Rubber Chem. Technol.* **1999**, *72*, 253.
[24] V. Trujillo, J. Kim, R. C. Hayward, *Soft Matter* **2008**, *4*, 564.
[25] W. Hong, X. H. Zhao, Z. G. Suo, *Appl. Phys. Lett.* **2009**, *95*, 3.
[26] E. Sultan, A. Boudaoud, *Phys. Rev. Lett.* **2006**, *96*, 4.
[27] G. Reiter, *Phys. Rev. Lett.* **1992**, *68*, 75.
[28] P. G. Saffman, G. Taylor, *Proc. R. Soc. London, Ser. A* **1958**, *245*, 312.
[29] A. Ghatak, M. K. Chaudhury, V. Shenoy, A. Sharma, *Phys. Rev. Lett.* **2000**, *85*, 4329.
[30] W. Monch, S. Herminghaus, *Europhys. Lett.* **2001**, *53*, 525.
[31] A. A. Golovin, S. H. Davis, P. W. Voorhees, *Phys. Rev. E* **2003**, *68*, 11.
[32] R. L. Jones, T. J. Hu, C. L. Soles, E. K. Lin, R. M. Reano, D. M. Casa, *Nano Lett.* **2006**, *6*, 1723.
[33] V. Shenoy, A. Sharma, *Phys. Rev. Lett.* **2001**, *86*, 119.
[34] G. M. Homsy, *Annu. Rev. Fluid Mech.* **1987**, *19*, 271.
[35] E. Sultan, A. Boudaoud, M. Ben Amar, *J. Fluid Mech.* **2005**, *543*, 183.
[36] M. Gonuguntla, A. Sharma, *Langmuir* **2004**, *20*, 3456.
[37] J. Nittmann, G. Daccord, H. E. Stanley, *Nature* **1985**, *314*, 141.
[38] H. van Damme, F. Obrecht, P. Levitz, L. Gatineau, C. Laroche, *Nature* **1986**, *320*, 731.
[39] Y. Couder, N. Gerard, M. Rabaud, *Phys. Rev. A* **1986**, *34*, 5175.
[40] E. Schäffer, T. Thurn-Albrecht, T. P. Russell, U. Steiner, *Nature* **2000**, *403*, 874.
[41] Z. Q. Lin, T. Kerle, S. M. Baker, D. A. Hoagland, E. Schaffer, U. Steiner, T. P. Russell, *J. Chem. Phys.* **2001**, *114*, 2377.
[42] M. Guvendiren, S. Yang, J. A. Burdick, *Adv. Funct. Mater.* **2009**, *19*, 3038.
[43] E. Southern, A. G. Thomas, *J. Polym. Sci. A* **1965**, *3*, 641.
[44] H. Tanaka, H. Tomita, A. Takasu, T. Hayashi, T. Nishi, *Phys. Rev. Lett.* **1992**, *68*, 2794.
[45] J. S. Sharp, R. A. L. Jones, *Phys. Rev. E* **2002**, *66*, 9.
[46] E. Sultan, A. Boudaoud, *J. Appl. Mech.-Trans. ASME* **2008**, *75*, 5.
[47] T. Tanaka, D. J. Fillmore, *J. Chem. Phys.* **1979**, *70*, 1214.
[48] A. Onuki, *J. Phys. Soc. Jpn.* **1988**, *57*, 703.
[49] T. Hwa, M. Kardar, *Phys. Rev. Lett.* **1988**, *61*, 106.
[50] S. J. Kwon, J. G. Park, S. H. Lee, *J. Chem. Phys.* **2005**, *122*, 4.
[51] Z. Y. Huang, W. Hong, Z. Suo, *J. Mech. Phys. Solids* **2005**, *53*, 2101.
[52] W. Hong, X. H. Zhao, Z. G. Suo, *J. Appl. Phys.* **2008**, *104*, 4.
[53] W. Hong, X. H. Zhao, J. X. Zhou, Z. G. Suo, *J. Mech. Phys. Solids* **2008**, *56*, 1779.
[54] D. Breid, A. J. Crosby, *Soft Matter* **2009**, *5*, 425.
[55] J. Y. Chung, A. J. Nolte, C. M. Stafford, *Adv. Mater.* **2009**, *21*, 1358.
[56] M. Guvendiren, S. Yang, J. A. Burdick, *Soft Matter* **2010**, *6*, 2044.
[57] P. C. Lin, S. Yang, *Appl. Phys. Lett.* **2007**, *90*, 241903.
[58] C. M. Stafford, S. Guo, C. Harrison, M. Y. M. Chiang, *Rev. Sci. Instrum.* **2005**, *76*, 5.
[59] C. M. Stafford, K. E. Roskov, T. H. Epps, M. J. Fasolka, *Rev. Sci. Instrum.* **2006**, *77*, 7.
[60] M. A. Biot, *J. Appl. Mech.* **1937**, *4*, A1.
[61] G. S. Gough, C. F. Elam, N. A. D. Bruyne, *J. R. Aeronaut. Soc.* **1940**, *44*, 12.
[62] N. Bowden, W. T. S. Huck, K. E. Paul, G. M. Whitesides, *Appl. Phys. Lett.* **1999**, *75*, 2557.
[63] J. Groenewold, *Phys. A* **2001**, *298*, 32.
[64] H. G. Allen, *Analysis and Design of Structural Sandwich Panels*, Pergamon Press, Oxford **1969**.
[65] J. W. Hutchinson, M. D. Thouless, E. G. Liniger, *Acta Metall. Mater.* **1992**, *40*, 295.
[66] H. Q. Jiang, D. Y. Khang, J. Z. Song, Y. G. Sun, Y. G. Huang, J. A. Rogers, *Proc. Natl. Acad. Sci. USA* **2007**, *104*, 15607.
[67] X. Chen, J. W. Hutchinson, *Scr. Mater.* **2004**, *50*, 797.
[68] E. P. Chan, A. J. Crosby, *Soft Matter* **2006**, *2*, 324.
[69] A. Baffoun, H. Haidara, D. Dupuis, P. Viallier, *Langmuir* **2007**, *23*, 9447.
[70] K. Efimenko, M. Rackaitis, E. Manias, A. Vaziri, L. Mahadevan, J. Genzer, *Nat. Mater.* **2005**, *4*, 293.
[71] R. C. Hayward, B. F. Chmelka, E. J. Kramer, *Macromolecules* **2005**, *38*, 7768.
[72] A. Ghatak, A. L. Das, *Phys. Rev. Lett.* **2007**, *99*, 4.
[73] J. Kim, J. Yoon, R. C. Hayward, *Nat. Mater.* **2010**, *9*, 159.
[74] R. G. Flemming, C. J. Murphy, G. A. Abrams, S. L. Goodman, P. F. Nealey, *Biomaterials* **1999**, *20*, 573.
[75] L. Hoipkemeier-Wilson, J. Schumacher, M. Carman, A. Gibson, A. Feinberg, M. Callow, J. Finlay, J. Callow, A. Brennan, *Biofouling* **2004**, *20*, 53.
[76] M. A. Meitl, Z. T. Zhu, V. Kumar, K. J. Lee, X. Feng, Y. Y. Huang, I. Adesida, R. G. Nuzzo, J. A. Rogers, *Nat. Mater.* **2006**, *5*, 33.
[77] M. Pretzl, A. Schweikart, C. Hanske, A. Chiche, U. Zettl, A. Horn, A. Boker, A. Fery, *Langmuir* **2008**, *24*, 12748.
[78] J. N. Israelachvili, *Intermolecular and Surface Forces*, Academic Press, New York **1992**.
[79] A. N. Gent, *Langmuir* **1996**, *12*, 4492.
[80] S. Minko, M. Muller, M. Motornov, M. Nitschke, K. Grundke, M. Stamm, *J. Am. Chem. Soc.* **2003**, *125*, 3896.
[81] T. L. Sun, G. J. Wang, L. Feng, B. Q. Liu, Y. M. Ma, L. Jiang, D. B. Zhu, *Angew. Chem. Int. Ed.* **2004**, *43*, 357.
[82] Y. Yao, X. Dong, S. Hong, H. Ge, C. C. Han, *Macromol. Rapid Commun.* **2006**, *27*, 1627.
[83] Y. F. Zhou, T. Yi, T. C. Li, Z. G. Zhou, F. Y. Li, W. Huang, C. H. Huang, *Chem. Mater.* **2006**, *18*, 2974.

[84] G. P. Li, T. Chen, B. Yan, Y. Ma, Z. Zhang, T. Yu, Z. X. Shen, H. Y. Chen, T. Wu, *Appl. Phys. Lett.* **2008**, *92*.
[85] T. N. Krupenkin, J. A. Taylor, T. M. Schneider, S. Yang, *Langmuir* **2004**, *20*, 3824.
[86] K. Khare, S. Herminghaus, J. C. Baret, B. M. Law, M. Brinkmann, R. Seemann, *Langmuir* **2007**, *23*, 12997.
[87] W. R. Hansen, K. Autumn, *Proc. Nat. Acad. Sci. USA* **2005**, *102*, 385.
[88] A. B. D. Cassie, S. Baxter, *Trans. Farad. Soc.* **1944**, *40*, 0546.
[89] W. Barthlott, C. Neinhuis, *Planta* **1997**, *202*, 1.
[90] L. Dong, A. K. Agarwal, D. J. Beebe, H. R. Jiang, *Nature* **2006**, *442*, 551.
[91] T. Krupenkin, S. Yang, P. Mach, *Appl. Phys. Lett.* **2003**, *82*, 316.
[92] N. Chronis, G. L. Liu, K. H. Jeong, L. P. Lee, *Opt. Express* **2003**, *11*, 2370.
[93] H. W. Ren, Y. H. Fan, S. T. Wu, *Opt. Lett.* **2004**, *29*, 1608.
[94] K. S. Hong, J. Wang, A. Sharonov, D. Chandra, J. Aizenberg, S. Yang, *J. Micromech. Microeng.* **2006**, *16*, 1660.